

Solvent-Free Mechano-Thermal Synthesis of a Li-Zn Phosphonate Cathode Framework

Augustin Ramackers, Darsi Rambabu,* Tom Goossens, Vasudeva Rao Bakuru, Petru Apostol, Robert Markowski, Géraldine Chanteux, Andrii Kachmar, Viliam Frano, Guillaume Esser, Nicolas Malherbe, Yan Zhang, Fabio Lucaccioni, Yaroslav Filinchuk, and Alexandru Vlad*

We dedicate this work to God, with gratitude and reverence

A key challenge in synthesizing alkali-ion metal–organic frameworks (MOFs) lies in the multistep procedures typically required, often involving solvothermal crystallization, desolvation, post-synthetic alkali-metalation, and controlled drying. To address this, a solvent-free mechano-thermal method is reported that combines solid-state grinding of precursors with thermal annealing under vacuum. This direct, scalable route offers a more sustainable alternative while enabling stoichiometric precision. We demonstrate this approach for the synthesis of $\text{Li}_4\text{-Zn-}p\text{-DOBPD}_{\text{mt}}$

(LZP^3 ; $p\text{-DOBPD}^{6-}$ = 2,5-dioxido-1,4-benzenediphosphate), in which lithium is incorporated during MOF formation. The resulting material exhibits better crystallinity compared to its conventionally synthesized counterpart and retains its key functional properties, including a reversible capacity of 130 mAh g^{-1} at 3.2 V versus Li^+/Li and a quasi-solid-state ionic conductivity of $10^{-6} \text{ S cm}^{-1}$ at 303 K. These results underscore the viability of solid-state synthesis for constructing alkali-ion-containing organic electrode materials with reduced processing complexity.

1. Introduction

Metal–organic frameworks (MOFs) are promising electrode materials for next-generation electrochemical energy storage due to their structural tunability, compositional versatility, and stability.^[1–7] Their ability to store charges via both metal centers and organic ligands contributes to high gravimetric energy densities.^[8,9] The porous nature facilitates efficient ion transport, while the extended framework provides cycling stability.^[7] MOFs can be tailored for electronic, ionic, or mixed conductivity, reducing the need of conductive additives and supporting rapid charge-discharge kinetics.^[1,7,10,11] In alkali-ion storage, they have been investigated as both cathodes and anodes.^[3–6,10,12,13] While anodes can achieve high capacities, challenges remain in optimizing redox potential, minimizing voltage hysteresis, and improving the Coulombic efficiency of the first-cycle.^[4,6] Developing MOF-based cathodes is more complex, requiring careful structural and compositional adjustments to enhance electrochemical properties.

Despite progress in MOF-based cathodes, alkali-ion-containing MOFs are still limited.^[1,2,7] Their redox activity typically

stems from either the anionic framework or metal nodes, while alkali cations primarily act as charge compensators. Only a few such MOFs have been reported, emphasizing the need for further investigation. One of the earliest examples, $\text{Li}_2\text{-M-DOBDC}$ ($\text{M} = \text{Mn, Mg}$),^[1] exhibited a one-electron redox process per ligand at 3.2 V versus Li^+/Li . Structurally, $\text{Li}_2\text{-Mn-DOBDC}$ is closely related to $\text{Mg}(\text{Li}_2)\text{-p-DHT}$,^[14] whereas $\text{Li}_2\text{-Mg-DOBDC}$ ^[1] adopts a different polymorph. The $\text{Li}_2\text{-Mn-DOBDC}$ MOF demonstrated a conductivity of $10^{-7} \text{ S cm}^{-1}$ at 293 K, significantly higher than its Mg analog, highlighting the influence of redox-active metal ions. Later, $\text{Li}_x\text{-M-(O)-DOBDC}$ ($\text{M} = \text{Al}^{3+}, \text{Fe}^{3+}$) incorporated trivalent metals, forming $\text{Li}_3\text{-M-(O)-(DOBDC)}$ or MIL-53(M)-(OLi)_2 ^[2] revealed a slightly lower redox potential of 2.76 V versus Li^+/Li . Recently, hexa anionic para-phosphono-phenolate-based ($\text{P}^3 = p\text{-DOBPD}^{6-}$ = 2,5-dioxido-1,4-benzenediphosphate) linker have emerged as a promising alternative, a study on $\text{Li}_4\text{-Zn-}p\text{-DOBPD}$,^[7] containing a non redox-active metal, supports a two-electron redox process per ligand at 3.2 V versus Li^+/Li . It also exhibits Li-ion conductivity ($10^{-5} \text{ S cm}^{-1}$ at 303 K), advancing MOF-based cathode materials. However, limitations persist, including improving electronic conductivity, enhancing alkali-ion transport, and stabilizing high-voltage redox processes.

A key challenge in synthesizing alkali-ion-containing MOFs,^[1,2,7] metal–organic compounds (e.g., $\text{Li}_2\text{-M-p-DHT}$),^[14] and coordination polymers (e.g., $\text{Li}_2\text{-Co-PTtSA}$),^[15] lies in the multistep process, which typically involves MOF synthesis, desolvation, alkali-metalation, and drying. These steps often require solvents and careful optimization. In particular, proton exchange in polyanionic frameworks typically requires strong bases ($\text{pK}_a > 14$), but solvent-based alkaliation often remains challenging^[2,7] due to equilibrium constraints

A. Ramackers, D. Rambabu, T. Goossens, V. R. Bakuru, P. Apostol, R. Markowski, G. Chanteux, A. Kachmar, V. Frano, G. Esser, N. Malherbe, Y. Zhang, F. Lucaccioni, Y. Filinchuk, A. Vlad

Institute of Condensed Matter and Nanosciences

Université catholique de Louvain

1348 Louvain-la-Neuve, Belgium

E-mail: rambabu.darsi@uclouvain.be
alexandru.vlad@uclouvain.be

Supporting information for this article is available on the WWW under <https://doi.org/10.1002/batt.202500426>

and possible reversibility. To simplify the synthesis, address metalation challenges and eliminate solvent use, a mechano-thermal approach can be employed, wherein the formation of volatile byproducts and subsequent thermal treatment under vacuum drive the reaction toward the desired metallated products. Herein, we apply the mechano-thermal approach to synthesize LZP³ ($\text{Li}_4\text{-Zn-}p\text{-DOB DP}_{\text{mt}}$), achieving direct lithiation during MOF formation, as confirmed by X-ray diffraction (XRD). This method enhances crystallinity while delivering comparable electrochemical performance (130 mAh g^{-1} at 3.2 V vs. Li^+/Li) and quasi-solid-state ionic conductivity ($10^{-6} \text{ S cm}^{-1}$). While this approach is promising for electrode material synthesis, parameters such as annealing temperature and precursor selection must be carefully optimized due to the unidirectional reaction pathway.

This one-step, solvent-free solid-state process offers a sustainable alternative while enabling precise stoichiometric control (Scheme 1 and S1, Supporting Information). Additionally, it circumvents challenges associated with conventional solvothermal methods, such as high solvent consumption, extended reaction times, and limited scalability. However, this approach is restricted to metal salts or bases that generate volatile byproducts, necessitating careful precursor selection.^[16]

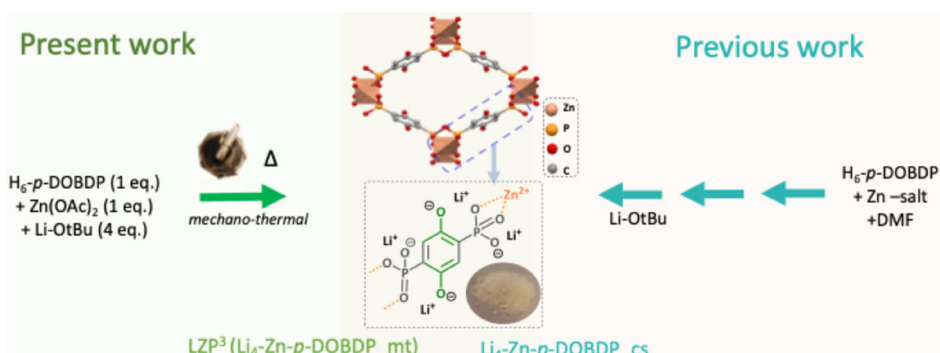
2. Results and Discussion

2.1. Synthesis, Physicochemical Analysis of LZP³

A solvent-free, mechano-thermal approach was employed to synthesize LZP³ (Scheme 1, left). Lithium tert-butoxide (Li-OtBu) was chosen as the Li source due to its melting point being within the range of ligand degradation range, making it suitable for solid-state synthesis. Various Zn precursors were tested, including diethylzinc (Zn(Et)_2), Zn-metal nano powder, and zinc acetate [Zn(OAc)_2]. Initially, LZP³ was synthesized using a 4:1:1 molar ratio of $\text{Li:Zn:H}_6\text{-}p\text{-DOB DP}$, while varying the Zn precursor (Table S1, Supporting Information). The extent of H-metal exchange (i.e., coordination of Zn and Li) was monitored by Fourier transform infrared (FT-IR) spectroscopy, with successful metalation indicated by the disappearance of the O—H stretching band at 3300 cm^{-1} , corresponding to phenolic and phosphonic —OH groups. Diethylzinc and Zn-nanopowder resulted in partial

deprotonation, indicating an incomplete reaction (Figure 1A). In contrast, the use of Zn(OAc)_2 led to complete disappearance of the O—H stretching band, signifying full deprotonation and effective metalation. The FT-IR spectrum of the sample synthesized using Zn(OAc)_2 closely resembles that of the conventionally synthesized MOF prepared in solution ($\text{Li}_4\text{-Zn-}p\text{-DOB DP}_{\text{cs}}$) (Table S1, Supporting Information, Figure 1A). The Powder XRD (PXRD) pattern of LZP³ is analogous to the reported material $\text{Li}_4\text{-Zn-}p\text{-DOB DP}_{\text{cs}}$, presenting several intensity variations of the main diffraction peaks. For instance, the peak at $5.7^\circ 2\theta$ exhibits significantly higher intensity, while others such as those at 9.7 and 10.1° , show improved resolution due to peak separation. Overall, the resulting diffractogram indicates improved crystallinity, likely due to fewer structural defects and possible preferred orientation of the structure (Figure 1B and 2A).

The effect of grinding time was evaluated between 10 and 30min, with FT-IR spectra showing comparable features across the range (Figure S1, Supporting Information). Based on these observations, a grinding time of 15 min was considered as optimal. The influence of pelletization was subsequently assessed by comparing samples pelletized under 4 tons of pressure for 3 min with those subjected to manual grinding for 15 min. XRD analyses indicated that both approaches led to the formation of the same phase. While the XRD peak positions remained consistent, a slight increase in peak intensity was observed for the pelletized sample, suggesting marginally improved crystallinity (Figure 1B). Further, effective metalation was further assessed by inductively coupled plasma optical emission spectroscopy (ICP-OES), confirming successful solid-state lithiation (Table S2, Supporting Information). The analysis revealed a Zn-to-Li ion ratio of 1:3.69, which is slightly lower than both the expected ratio (1:4) and the initial precursor ratio. This discrepancy can be attributed to the tendency of lithium tert-butoxide (Li-OtBu) sublimation during the reaction. To compensate this loss, we introduced a slight excess of 4.5 equivalents of Li-OtBu relative to Zn (instead of 4 equivalents required for the stoichiometric ratio). Under these conditions, ICP-OES showed an improved Zn-to-Li ratio of 1:3.93. Furthermore, to improve lithiation efficiency and demonstrate the flexibility of the method, we explored a sequential approach. The reaction was first performed with 4 equivalents of Li-OtBu to yield ($\text{L}_{3.69}\text{ZP}^3$). Then, an additional 0.5 equivalents of Li-OtBu was added before a second grinding and heating step to compensate



Scheme 1. Comparison of synthesis routes, highlighting the present solid-state mechano-thermal method (left) versus conventional MOF-based approach (right).

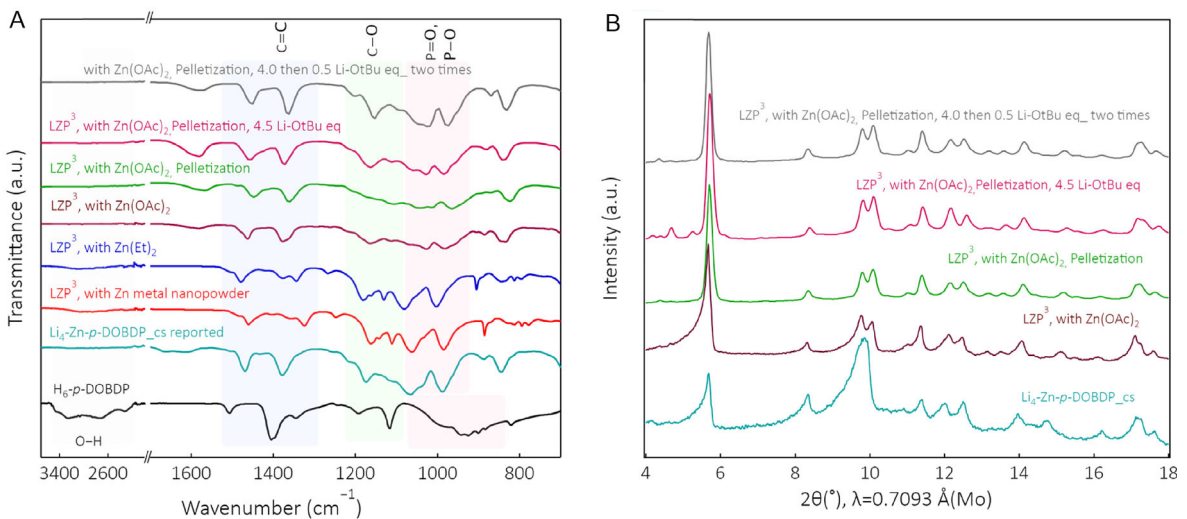


Figure 1. Optimization of the mechano-thermal synthesis of LZP^3 . A) FTIR spectra comparing different Zn precursors and synthetic conditions using $\text{Zn}(\text{OAc})_2$ for LZP^3 formation, shown alongside $\text{Li}_4\text{-Zn-p-DOBDP}_\text{cs}$ and the $\text{H}_6\text{-p-DOBDP}$ ligand. B) XRD patterns showing the effect of synthetic parameters using zinc acetate on LZP^3 formation, compared with $\text{Li}_4\text{-Zn-p-DOBDP}_\text{cs}$. All samples were ground for 15 min prior to thermal treatment.

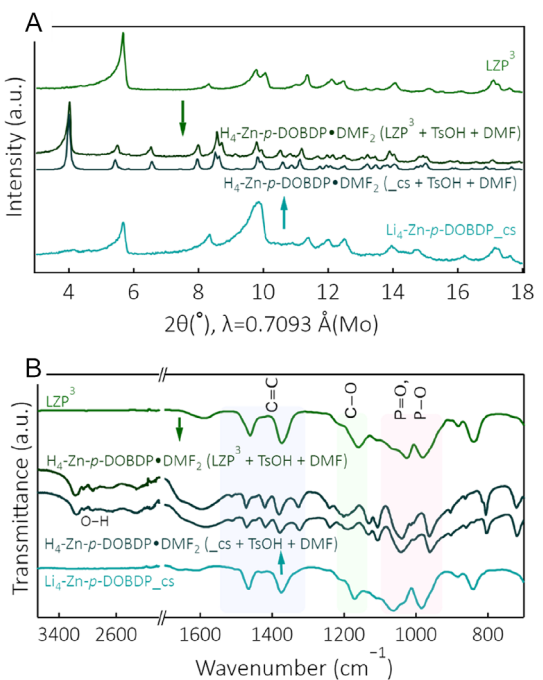


Figure 2. Reprotonation observations of $\text{Li}_4\text{-Zn-p-DOBDP}_\text{cs}$ and LZP^3 isoforms. A) XRD patterns and B) FT-IR spectra overlays of $\text{Li}_4\text{-Zn-p-DOBDP}_\text{cs}$, $\text{L}_{3.69}\text{ZP}^3$ and their reprotonated MOFs, and $\text{H}_4\text{-Zn-p-DOBDP-DMF}_2$.

for any lithium loss during processing. ICP-OES analysis confirmed enhanced lithiation, with the Zn-to-Li ratio increasing to 1:3.98.

The similarity in FT-IR and XRD patterns among $\text{Li}_{3.69}\text{ZP}^3$ (4 eq. of Li-OtBu used), $\text{Li}_{3.93}\text{ZP}^3$ (4.5 eq. of Li-OtBu used), and $\text{Li}_{3.98}\text{ZP}^3$ (4 + 0.5 eq. of Li-OtBu used in two steps) suggests the formation of the same structure, despite a difference of approximately 0.3 equivalents of Li per Zn ion (Figure 1 and Table S2, Supporting Information). However, in samples where excess Li-OtBu (4.5 equiv.) was used, either in a single step or sequentially, a

minor additional peak appeared around 5° 2θ (Figure 1B), which may be attributed to unidentified phase impurities. Among these, $\text{L}_{3.69}\text{ZP}^3$ (with 4.0 equivalents of Li-OtBu, 15 min of mechanical grinding, pelletized) was identified as the optimal composition, while others involved either two-step lithiation ($\text{Li}_{3.98}\text{ZP}^3$) or exhibited minor phase impurities ($\text{Li}_{3.93}\text{ZP}^3$). To identify more sustainable and cost-effective lithium precursors, ecofriendly alternatives, such as Li_2CO_3 , Li-OAc , and LiOH , were explored and compared with Li-OtBu. Mechanical grinding was carried out under ambient conditions without the use of an inert atmosphere, followed by drying in a vacuum oven. The resulting FTIR spectra indicate that the reaction was incomplete, as evidenced by a broad band around 3200 cm^{-1} corresponding to residual O-H stretching vibrations (Figure S2, Supporting Information).

Even though the FT-IR spectrum of the sample synthesized using Zn-acetate closely resembles that of the reported MOF, a notable difference is the presence of a band at 1600 cm^{-1} , which is likely attributed to a C=O stretching vibration introduced during the synthesis (Figure 1A). This suggests that the band originates from the residual acetate present within framework. To remove residual acetate, $\text{L}_{3.69}\text{ZP}^3$ was washed separately with DMF, THF, or methanol. Methanol washing effectively removed the acetate, as confirmed by the disappearance of the C=O band at 1600 cm^{-1} in the FT-IR spectrum (Figure S3A, Supporting Information). However, methanol washing also carries the risk of partial reprotonation due to its comparable pKa to that of the deprotonated sites in the framework. This reprotonation was confirmed by ICP-OES, showing a loss of lithium ion (Zn:Li ratio of 1:3.25, Table S2, Supporting Information). The loss of lithium could potentially influence electrochemical performance (*vide infra*, *Electrochemical Cycling section*). In contrast, THF and DMF washing did not alter the FT-IR spectrum, indicating no significant removal of residual acetate. PXRD analysis confirmed that the crystal structure remained unchanged after methanol washing (Figure S3B, Supporting Information), indicating that residual

acetate species are likely trapped within or surface of the framework and are not easily removed by conventional washing.

X-ray photoelectron spectroscopy (XPS) analysis of $L_{3.69}ZP^3$ further confirms the presence of zinc (Zn), oxygen (O), phosphorus (P), lithium (Li), and carbon (C) in the sample, indicating the presence of both the ligand and the metal ions Zn and Li. The binding energies of Zn and Li are consistent with their coordination to the oxygen atoms of the ligand (Figure S4, Supporting Information). Furthermore, crystallite size and morphology were examined using scanning electron microscopy (SEM) of $Li_4\text{-Zn-}p\text{-DOB DP_cs}$ synthesized under different conditions: without pelletization, with pelletization followed by methanol washing, and with 4.5 equivalents of Li-OtBu. All samples exhibit similar morphologies, consisting of near-spherical particles ranging from $\approx 0.5\text{--}2\ \mu\text{m}$, forming aggregated structures (Figure S5, Supporting Information). These results suggest that the morphology remains largely unaffected by pelletization, excess lithiation, or post-synthetic methanol washing. In contrast, the reported ($Li_4\text{-Zn-}p\text{-DOB DP_cs}$) MOF^[7] displays tends toward more plate- or rod-like particles of around $1\ \mu\text{m}$ in size. These morphological differences may subtly influence key material properties, such as crystallinity (XRD features), electrochemical behavior, and ionic conductivity.

To further confirm the isomorphous nature $Li_{3.93}ZP^3$ to the $Li_4\text{-Zn-}p\text{-DOB DP_cs}$, the material was treated with 4 equivalents of *p*-toluenesulfonic acid (TsOH) in DMF to induce reprotonation and resolvation. This treatment yielded a solvated crystalline MOF, $H_4\text{-Zn-}p\text{-DOB DP-DMF}_2$, whose FT-IR and PXRD patterns matched those of the conventionally synthesized material (Figure 2A,B). This confirmed that the framework obtained through solid-state synthesis is isostructural to the previously reported one, with improved crystallinity. A shift in the low-angle peak from 5.7° in ZP^3 to 4.0° in $H_4\text{-Zn-}p\text{-DOB DP-DMF}_2$ suggests a contraction of the framework in ZP^3 , consistent with the behavior of $Li_4\text{-Zn-}p\text{-DOB DP_cs}$. Also, profile fitting further confirms reduced unit cell dimensions along the *a*, *b*, and *c* axes in ZP^3 compared to $H_4\text{-Zn-}p\text{-DOB DP-DMF}_2$. These observations indicate that ZP^3 adopts a more compact framework (Table S3 and Figure S6, Supporting Information, a trend that may also be applicable to the isomorph $Li_4\text{-Zn-}p\text{-DOB DP_cs}$). Additionally, nitrogen adsorption isotherm measurements on $L_{3.69}ZP^3$ displayed a type-I adsorption profile with a Brunauer-Emmett-Teller surface area of $11\text{ m}^2\text{ g}^{-1}$ (Figure S7, Supporting Information), further suggesting a more compact framework, as also indicated by the low-angle peak shift to higher 2θ in the XRD pattern.

2.2. Ionic Conductivity of ZP^3

Motivated by the ionic conductivity reported for lithium-rich $Li_4\text{-Zn-}p\text{-DOB DP_cs}$, which is crucial for charge-discharge kinetics, we further measured the ionic conductivity of ZP^3 using potentiostatic electrochemical impedance spectroscopy (PEIS) with a two-probe cold-pressed pellet set-up. No ionic conductivity was observed in the pure solid state, while the reported value for $Li_4\text{-Zn-}p\text{-DOB DP_cs}$ is 10^{-8} S cm^{-1} . However, at 303 K and under inert conditions in the quasi-solid state (refer

Table 1. Quasi solid Li-ion conductivity, and activation energy of ZP^3 and $Li_4\text{-Zn-}p\text{-DOB DP_cs}$.

Entry	σ , [$S\text{ cm}^{-1}$] ^a With PC	E_a , [eV] ^b
$Li_{3.69}ZP^3$ (with 4 eq. Li-OtBu)	1.4×10^{-6}	0.24
$Li_{3.93}ZP^3$ (with 4.5 eq. Li-OtBu)	1.2×10^{-6}	0.20
$Li_4\text{-Zn-}p\text{-DOB DP_cs}$ (reported) ^[7]	2.7×10^{-5}	0.16

^aIonic conductivity at 303 K; ^bActivation energy.

Experimental Section for details), the ionic conductivity of ZP^3 was found to be 10^{-6} S cm^{-1} (Table 1), which is one order of magnitude lower than the reported values. Variable-temperature PEIS results (Figure 3) for $Li_{3.69}ZP^3$ and $Li_{3.93}ZP^3$, show a comparable activation energy (E_a) of 0.24, and 0.20 eV, respectively (Figure 3A and Table 1). These E_a values are slightly higher than those reported, indicating that the ZP^3 samples exhibit marginally lower conductivity, possibly due to morphological differences (Figure S5, Supporting Information)

2.3. Electrochemical Evaluation of ZP^3

The ZP^3 samples with different contents of lithium, optimized through synthesis adjustments, were evaluated in Li-half cell configurations. The material has a theoretical capacity of 150 mAh g^{-1} , corresponding to a $2e^-$ redox process. The previously reported $Li_4\text{-Zn-}p\text{-DOB DP_cs}$ exhibited a specific capacity of 140 mAh g^{-1} ($1.86e^-$) at an average potential of 3.2 V versus Li^+/Li (Figure 4A).^[7] The first optimized sample, $L_{3.69}ZP^3$, demonstrated an average potential of 3.2 V versus Li^+/Li , delivering a specific capacity of 130 mAh g^{-1} , corresponding to $1.72e^-$ (Figure 4B). In contrast to $L_{3.69}ZP^3$ material, $L_{3.99}ZP^3$ and $L_{3.93}ZP^3$ exhibited specific capacities of 131 and 70 mAh g^{-1} , corresponding to 1.75 and $0.9e^-$ per formula unit (Figure S8A, B, Supporting Information). These results indicate that the addition of excess lithium source during synthesis does not enhance electrochemical performance.

Despite the presence of residual acetate in $L_{3.69}ZP^3$, electrochemical cycling remained stable, indicating that post-synthetic washing is unnecessary, and that trace acetate does not significantly affect the electrochemical performance. In fact, methanol washing led to a nearly 50% decrease in capacity, attributed to lithium loss (Figure S8C, Supporting Information). Among the samples, $L_{3.69}ZP^3$ exhibited the most favorable electrochemical response. Nevertheless, its capacity remained slightly lower ($\approx 9\%$) than that of the conventionally synthesized $Li_4\text{-Zn-}p\text{-DOB DP_cs}$. Li-half cells were tested at a 0.025 C rate, in contrast to the 0.1 C rate previously reported for $Li_4\text{-Zn-}p\text{-DOB DP_cs}$. Additionally, 20% less carbon was used in the $L_{3.69}ZP^3$ electrode formulation to align with practical material loading considerations.

To ensure a more complete capacity response, a lower C-rate was employed, as electrochemical behavior can be influenced by factors such as morphology, particle size, and crystallinity.^[17] While $L_{3.69}ZP^3$ shows improved crystallinity, it exhibits kinetic limitations likely related to its particle morphology and size distribution, which may hinder ion transport and contribute to a modest reduction in capacity. Ionic conductivity measurements further

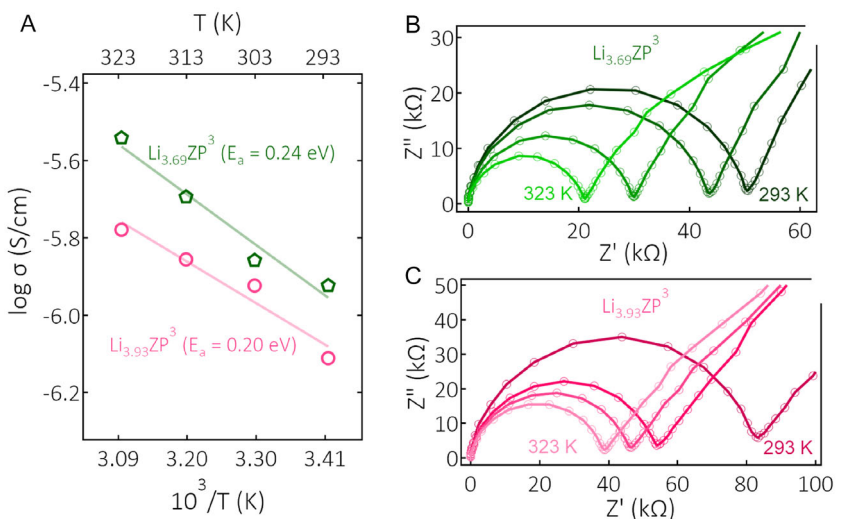


Figure 3. Variable-temperature ionic conductivity plots for LZP³. A) Arrhenius plots with corresponding activation energies (E_a). B,C) PEIS results for Li_{3.69}ZP³ and Li_{3.93}ZP³, respectively.

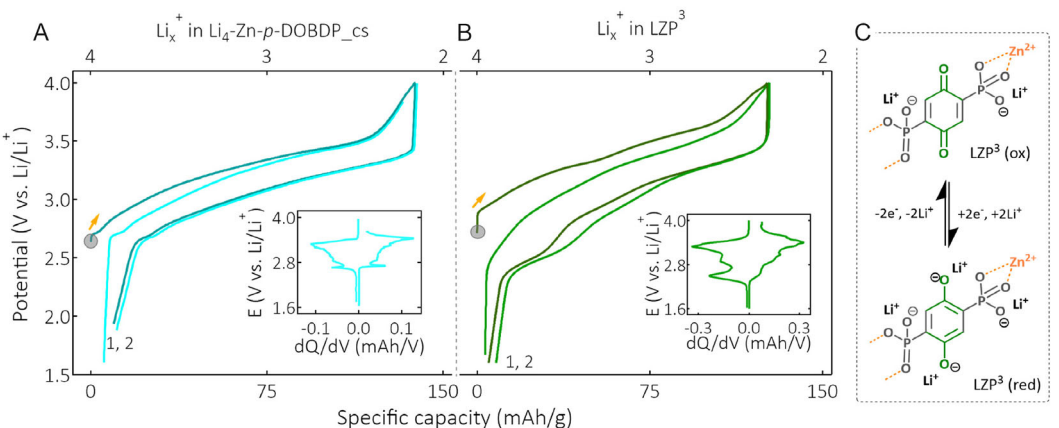


Figure 4. Electrochemical performance comparison of Li₄-Zn-p-DOBDP_{cs} and L_{3.69}ZP³. Potential–composition profiles of reported A) Li₄-Zn-p-DOBDP_{cs} and B) L_{3.69}ZP³, measured in Li-metal half-cells, are shown along with their corresponding differential capacity (dQ/dV) plots as insets. For the L_{3.69}ZP³ electrode, a galvanostatic rate corresponding to a one-electron exchange per formula unit over 20 h (0.025 C) was applied. Electrodes were composed of 60 wt% active material, 30 wt% super P carbon (C65), and 10 wt% PTFE. The electrolyte used was LP30, consisting of 1 M LiPF₆ in a 1:1 (v/v) mixture of ethylene carbonate (EC) and dimethyl carbonate (DMC). C) Redox mechanism of L_{3.69}ZP³ during the charge (oxidation) and discharge (reduction).

suggest that limited ionic transport plays a significant role in the observed behavior. Specifically, L_{3.69}ZP³ displays lower ionic conductivity than Li₄-Zn-p-DOBDP_{cs}, which likely contributes to its reduced electrochemical response. This difference is supported by SEM analyses, which reveal that L_{3.69}ZP³ possesses a broader range of particle morphologies and crystallite sizes compared to Li₄-Zn-p-DOBDP_{cs} (Figure S5, Supporting Information).

Further, post-cycling characterization after 20 cycles at 0.1 C confirms the structural and compositional stability of the L_{3.69}ZP³ electrode (Figure S9, Supporting Information). SEM and energy-dispersive X-ray spectroscopy analyses show unchanged morphology and retention of key elements (Zn, P, O, Li, and C). XRD patterns remain consistent, and visual inspection shows no signs of dissolution. These results indicate stable and reversible redox behavior, consistent with the quinone-based redox mechanism (Figure 4C).^[7]

2.4. Rate and Cycling Capability of LZP³

To assess potential kinetic limitations, C-rate tests were performed. Benefiting from its quasi-solid ionic conductivity, L_{3.69}ZP³ demonstrated competitive rate performance, retaining 130 mAh g⁻¹ at a low charge–discharge rate of 0.025 C. Increasing the rate to 0.05, 0.1, 0.2, 0.5, and 1 C resulted in specific capacities of 120, 109, 100, 78, and 69 mAh g⁻¹, respectively (Figure 5A and S10, Supporting Information). The gradual decrease in capacity at higher rates suggests that kinetic limitations, likely influenced by ion transport pathways, play a role in the material's rate-dependent behavior. The L_{3.69}ZP³ material exhibited good cycling stability, retaining over 99% of its initial capacity after 50 cycles at a rate of 0.2 C (Figure 5B). Even at a higher rate of 1 C, L_{3.69}ZP³ retained 67 mAh g⁻¹ after 100 cycles, suggesting good stability at higher C-rates, with the lower

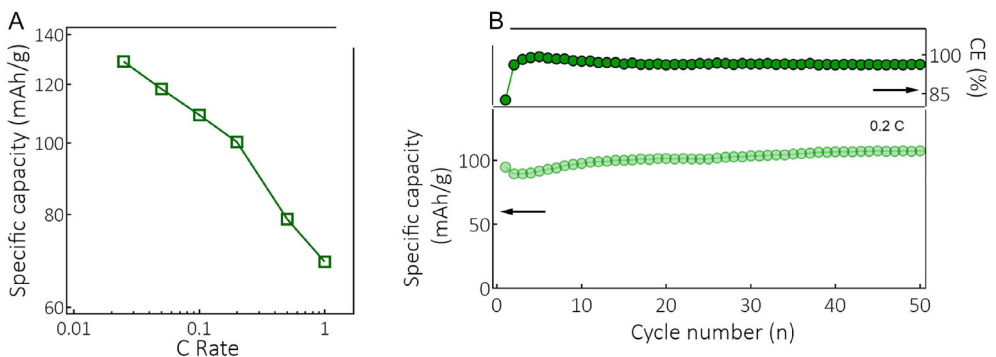


Figure 5. A) Rate capability at C-rates ranging from 0.025 to 1 C, showing specific discharge capacity (mAh g^{-1}) averaged over five cycles at each C-rate, and B) cycling performance at 0.2 C of the $\text{L}_{3.69}\text{ZP}^3$ electrode in Li-metal half-cell configurations. Electrodes are composed of 60 wt% active material, 30 wt% super P carbon, and 10 wt% PTFE, using LP30 electrolyte.

capacity compared to lower C-rates likely due to kinetic limitations (Figure S11, Supporting Information). This stability is primarily attributed to the insoluble, polyanionic, and polymeric nature of the $\text{L}_{3.69}\text{ZP}^3$ framework, which helps prevent dissolution.

3. Conclusion

We have demonstrated a solvent-free solid-state approach for alkali-ion-containing MOF, addressing the challenges associated with conventional multistep processes that typically require solvents and precise optimization. Using a mechano-thermal method, we successfully synthesized the Li-ion MOF ($\text{L}_{3.69}\text{ZP}^3$), achieving direct lithiation during MOF formation. This approach enhances the crystallinity of $\text{L}_{3.69}\text{ZP}^3$ while preserving its electrochemical performance (130 mAh g^{-1} at 3.2 V vs. Li^+/Li) and quasi-solid-state ionic conductivity ($10^{-6} \text{ S cm}^{-1}$, at 303 K), comparable to conventionally synthesized multistep methods. Beyond $\text{L}_{3.69}\text{ZP}^3$, this method may offer broader applicability to other transition-metal-based systems, making it a promising strategy for organic lithiation processes. These findings highlight the potential of solid-state synthesis in advancing alkali-ion-containing (metal-)organic cathode materials, offering a more sustainable and efficient route for next-generation energy storage applications.

4. Experimental Section

Materials (Chemicals and Reagents)

The following chemicals were used without further purification: 2,5-dihydroxy-1,4-benzenediphosphonic acid ($\text{H}_6\text{-p-DOBPP}$, 98%, Epsilon Chimie), zinc (II) acetate (99%, anhydrous, Thermo Scientific), lithium tert-butoxide (Li-OtBu , 97%, Sigma Aldrich), zinc nano powder (99%, Sigma Aldrich) diethylzinc (ca. 15% in Toluene, ca. 1 mol L⁻¹, TCI), methanol, THF, DMF solvents (anhydrous, Thermo Scientific), and polytetrafluoroethylene (PTFE, from Sigma Aldrich).

Physicochemical Characterization

FTIR spectroscopy was carried out using an Agilent Technologies Cary 630 FTIR spectrometer operated in transmission or ATR mode. PXRD

patterns were collected either on STOE DARMSTADT Transmission diffractometer system using Mo K α 1 radiation with a wavelength of 0.70930 Å or a MAR345 image-plate detector equipped with an Incoatec Mo ($\lambda = 0.71073$ Å) Microfocus ($1\mu\text{s}$ 2.0) X-ray source operating at 50 kV and 1000 μA . The resulting 2D images were azimuthally integrated using the Fit2D software, with LaB6 serving as a calibrant. The XRD samples were loaded into 0.7 mm glass capillaries (Hilgenberg GmbH). Nitrogen sorption measurements at 77 K were performed on a Micromeritics ASAP 2020 instrument after activating the sample at 180 °C under vacuum for 10 h. SEM images were acquired on Zeiss Neon 40 cross-beam workstation with Gemini SEM column (Carl Zeiss Iberia, S.L., Madrid, Spain). ICP-OES analysis was performed on Perkin Elmer Avio220 max. The samples for XPS analysis were made in an Ar-filled glovebox, where they were transferred to a vessel which was directly attached to the ultrahigh-vacuum system to avoid exposure to air. XPS measurements were carried out using the PHI Genesis Fully Automated Multi-Technique Scanning XPS/HAXPES Microprobe, with a Cr target operating at 5414.8 eV.

Synthesis of LZP³

The synthesis was carried out according to the protocol outlined below, with additional optimizations provided in the Supporting Information (SI). All manipulations were performed in an Ar-filled glove box. To a mortar, 1 equivalent of $\text{H}_6\text{-p-DOBPP}$ (0.2 mmol, 54 mg), 1 equivalent of Zn(OAc)_2 (0.2 mmol, 37 mg, dried at 180 °C, 5 h, prior to use), and 4 equivalents of LiOtBu (0.8 mmol, 64 mg) were added and ground for 15 min. The resulting powder was then pressed into a pellet (10 mm) under a pressure of 4 tons for 3 min (1 min per cycle, repeated 3 times). The obtained pellet was subsequently heated in a vacuum oven according to the following temperature program: 5 h at 160 °C, 8 h at 200 °C, and 4 h at 250 °C. After heating, the product, which was off-white, directly yielded the desired LZP³.

Ionic Conductivity Measurements

Approximately 20 mg of the powders, with 5 μL of propylene carbonate (PC), were cold-pressed under an applied pressure of 2 tons between two stainless steel rods (7 mm in diameter). These pellets were then placed in custom-designed Swagelok cells, under an inert atmosphere, with the cell locked to maintain the pressure. Variable-temperature conductivity measurements were conducted in a climatic chamber with continuous pressure applied. A Bio-Logic potentiostat was used for the conductivity measurements, which included PEIS over a frequency range of 7 MHz–10 mHz with a 200 mV amplitude AC signal. The ionic conductivity was calculated using the equation: $\sigma = L/(AR)$, where σ is the ionic conductivity,

L is the thickness of the pellet, A is the pellet area, and R is the resistance obtained from the PEIS data.

Electrochemical Li-Metal Half-Cell Assembly and Testing

LZP³ electrode materials were tested using a two-electrode configuration in 2032-type coin cells, assembled in an Ar-filled glove box. The positive working electrode (cathode) was prepared by hand-grinding 100 mg of Li₄-Zn-p-DOBDP_s active material (60 wt%) with 30 wt% Super-P carbon (C-65) and 10 wt% poly(tetrafluoroethylene) (PTFE) dry binder. Approximately 4 mg of the positive electrode composite was then applied onto the stainless-steel positive cell case and pressed directly onto the case using a stainless-steel rod. A glass fiber separator (19 mm diameter) was placed on top of the positive electrode, and 100 µL of electrolyte (1 M LiPF₆ in a 1:1 (v/v) mixture of ethylene carbonate and dimethyl carbonate [EC/DMC, LP30, battery-grade, Solvionic]) was added to soak the separator. The Li metal chip, serving as the counter and pseudo-reference electrode (anode), was placed on top of the separator. A stainless steel (316) current collector and spring were placed above the anode, and the cell was sealed with the negative case by applying 0.7 tons of pressure. Galvanostatic charge-discharge tests were conducted at room temperature using a Neware battery testing system.

Acknowledgements

The major core of the work was funded through FWO and F.R.S.-FNRS under the Excellence of Science program (EOS 40007515). Partial support was received from the European Research Council under the European Union's Horizon 2020 research and innovation program (grant agreement no. 770870, MOOIRe—A.V.) as well as F.R.S.-FNRS through F.4552.21-P grant D.R., B.V.R., and X.L. acknowledge F.R.S.-FNRS for Chargé de Recherche (CR) fellowship (grant agreement no. 40010410, 40023657, and 40010559). T.G., R.M., and G.C. acknowledge F.R.S.-FNRS for Ph.D. fellowships.

Conflict of Interest

The authors declare no conflict of interest.

Author Contributions

Augustin Ramackers: conceived and designed the project, Solid-state mechano-thermal approach was initiated and optimized, have performed the major part of the experimental work, involved in the unit cell parameter determination, performed conductivity measurements, involved in SEM analysis. **Darsi Rambabu:** conceived and designed the project, Solid-state mechano-thermal approach was initiated and optimized, have performed the major part of the experimental work, involved in the unit cell parameter determination, performed conductivity measurements. **Tom Goossens:** assisted by performed the major part of the experimental work, assisted by performed conductivity measurements. **Vasudeva Rao Bakuru:** assisted by performed the major part of the experimental work, assisted by performed conductivity measurements. **Petru Apostol:** assisted by performed the major part of the experimental work, assisted by performed

conductivity measurements. **Robert Markowski:** assisted by performed the major part of the experimental work, Fabio Lucaccioni involved in ICP analysis, involved in ICP analysis. **Géraldine Chanteux:** assisted by performed the major part of the experimental work, involved in SEM analysis. **Andrii Kachmar:** involved in XPS analysis. **Viliam Frano:** involved in XPS analysis. **Guillaume Esser:** involved in the unit cell parameter determination. **Nicolas Malherbe:** involved in the unit cell parameter determination. **Fabio Lucaccioni:** assisted by performed the major part of the experimental work, involved in ICP analysis. **Yaroslav Filinchuk:** involved in the unit cell parameter determination. **Viliam Frano:** involved in XPS analysis. **Alexandru Vlad:** conceived and designed the project. All authors made iterative contributions and changes to the experiments during implementation and subsequent analysis, working collaboratively as a team. All authors contributed to the scientific discussion of the results as well as participated in the writing and approved the manuscript.

Data Availability Statement

The data that support the findings of this study are available from the corresponding author upon reasonable request.

Keywords: ionic conductivity · Li-ion cathode · mechano-thermal approach · metal–organic frameworks · solid state synthesis

- [1] D. Rambabu, A. E. Lakaychi, J. Wang, L. Sieuw, D. Gupta, P. Apostol, G. Chanteux, T. Goossens, K. Robeyns, A. Vlad, *J. Am. Chem. Soc.* **2021**, *143*, 11641.
- [2] M. Denis, H. Chevreau, P. Salcedo-Abraira, P. Moreau, N. Dupré, M. Paris, P. Poizot, T. Devic, *Mol. Syst. Des. Eng.* **2023**, *8*, 1030.
- [3] Z. Zhang, K. Awaga, *MRS Bull.* **2016**, *41*, 883.
- [4] R. Zhao, Z. Liang, R. Zou, Q. Xu, *Joule* **2018**, *2*, 2235.
- [5] W. Wang, D. Chen, F. Li, X. Xiao, Q. Xu, *Chem* **2024**, *10*, 86.
- [6] V. Shrivastav, S. Sundriyal, P. Goel, H. Kaur, S. K. Tuteja, K. Vikrant, K. H. Kim, U. K. Tiwari, A. Deep, *Coord. Chem. Rev.* **2019**, *393*, 48.
- [7] Y. Zhang, J. Wang, P. Apostol, D. Rambabu, A. E. Lakaychi, X. Guo, X. Zhang, X. Lin, S. Pal, V. R. Bakuru, X. Chen, A. Vlad, *Angew. Chem., Int. Ed.* **2023**, *62*, e202310033.
- [8] Z. Zhang, H. Yoshikawa, K. Awaga, *J. Am. Chem. Soc.* **2014**, *136*, 16112.
- [9] M. E. Ziebel, C. A. Gaggioli, A. B. Turkiewicz, W. Ryu, L. Gagliardi, J. R. Long, *J. Am. Chem. Soc.* **2020**, *142*, 2653.
- [10] D. Sheberla, J. C. Bachman, J. S. Elias, C. J. Sun, Y. Shao-Horn, M. Dincă, *Nat. Mater.* **2017**, *16*, 220.
- [11] D. M. D'Alessandro, *Chem. Commun.* **2016**, *52*, 8957.
- [12] Z. Wang, H. Tao, Y. Yue, *ChemElectroChem* **2019**, *6*, 5358.
- [13] D.-Y. Wang, R. Liu, W. Guo, G. Li, Y. Fu, *Coord. Chem. Rev.* **2020**, *429*, 213650.
- [14] A. Jouhara, N. Dupré, A. C. Gaillot, D. Guyomard, F. Dolhem, P. Poizot, *Nat. Commun.* **2018**, *9*, 4401.
- [15] J. Wang, X. Guo, P. Apostol, X. Liu, K. Robeyns, L. Gence, C. Morari, J.-F. Gohy, A. Vlad, *Energy Environ. Sci.* **2022**, *15*, 3923.
- [16] V. R. Bakuru, P. Apostol, D. Rambabu, S. Pal, X. Lin, R. Markowski, T. Goossens, D. Tie, A. Kachmar, Y. Zhang, G. Chanteux, A. Vlad, *Energy Environ. Sci.* **2025**, *18*, 6131, <https://doi.org/10.1039/D4EE05701E>.
- [17] R. Russo, C. Davoisne, A. Urrutia, Y. Danten, C. Gatti, G. Toussaint, P. Stevens, C. Frayret, M. Becuwe, *ACS Appl. Polym. Mater.* **2023**, *5*, 9865.

Manuscript received: June 2, 2025
Revised manuscript received: August 10, 2025
Version of record online: